Theoretical Chemistry Accounts (2019) 138:76
https://doi.org/10.1007/s00214-019-2463-9

REGULAR ARTICLE

New insights into Fe–H_2 and Fe–H^- bonding of a [NiFe] hydrogenase mimic: a local vibrational mode study

Małgorzata Z. Makoś[1] · Marek Freindorf[1] · Daniel Sethio[1] · Elfi Kraka[1]

Received: 6 March 2019 / Accepted: 15 May 2019 / Published online: 24 May 2019

Abstract
In this work, we investigated the strength of the H^- and H_2 interaction with the Fe atom of a [NiFe] hydrogenase mimic, and how this interaction can be modulated by changing the Fe ligand in trans-position relative to H^- and H_2. We used as a quantitative measure of bond strength local vibrational force constants derived from the Konkoli–Cremer local mode analysis, complemented by the topological analysis of the electronic density and the natural bond orbital analysis. Seventeen different ligands were investigated utilizing density functional theory calculations, including σ-donor ligands such as CH_3^-, $C_2H_5^-$, NH_3, and H_2O, π-donor ligands such as Cl^-, F^-, and OH^-, and σ-donor/π-acceptor ligands such as CN^- and CO. According to the local mode analysis, Fe–H interactions are strengthened by σ-donor or π-donor ligands and weakened by σ-donor/π-acceptor ligands. In contrast, the H–H bond of H_2 is weakened by σ-donor or π-donor ligands and strengthened by σ-donor/π-acceptor ligands. We also present a new metal–ligand electronic parameter (MLEP) for Fe–H ligands which can be generally applied to evaluate the Fe–H bond strength in iron complexes and iron hydrides. These results form a valuable basis for future [NiFe] hydrogenase-based catalyst design and fine tuning, as well as for the development of efficient biomimetic catalysts for H_2 generation.

Keywords [NiFe] Hydrogenase mimic · [NiFe] Hydrogen · Hydride complexes · Local vibrational mode analysis · Local mode force constants · Metal–ligand electronic parameter (MLEP)

1 Introduction

Hydrogenases are metalloenzymes that efficiently catalyze the reversible oxidative cleavage of molecular hydrogen into two protons and two electrons [37, 85, 94, 109]. They are present in nature and widely found in bacteria, archaea, and some eukaryotes [136]. According to the metal atoms in the active site, hydrogenases can be classified into three types: [Fe], [FeFe], and [NiFe] hydrogenases [86]. [FeFe] and [NiFe] hydrogenases are active catalysts, while [Fe] hydrogenases are only activated in the presence of methenyltetrahydromethanopterin [44]. Due to their unique hetero-binuclear active site and superior oxygen tolerance, considerable attention has been directed toward the [NiFe] hydrogenases [10, 14, 82].

[NiFe] hydrogenases have been extensively investigated due to their importance in putative future hydrogen-based economy, such as bio-fuel, power cells, photocatalytic water splitting, and hydrogen sensors technologies [19, 32, 52, 61, 137]. They have remarkable catalytic properties, particularly low-over potential and high turnover power [30, 43, 108]. A significant number of computational studies have focused on the structural characterization [103], the catalytic mechanism [31, 47, 106, 107, 127, 134, 135], in particular, proton reduction [128], and the electronic structure [57, 122, 138] and oxidation states [11, 123] of the [NiFe] hydrogenase active site. Also, several models of the [NiFe] active site have been discussed that can mimic the chemical functions of the hydrogenase enzyme [59, 112].

Published as part of the special collection of articles derived from the 11th Congress on Electronic Structure: Principles and Applications (ESPA-2018).

Electronic supplementary material The online version of this article (https://doi.org/10.1007/s00214-019-2463-9) contains supplementary material, which is available to authorized users.

✉ Elfi Kraka
ekraka@gmail.com

[1] Computational and Theoretical Chemistry Group (CATCO), Department of Chemistry, Southern Methodist University, 3215 Daniel Avenue, Dallas, TX 75275-0314, USA

First [NiFe] hydrogenase models that exhibited H_2 producing activity were reported in 2005 [143]. More recent examples of [NiFe] hydrogenase models are structures with phosphines ligands on Ni that evolve hydrogen [7, 8, 15] and structures with thiolate ligands bonded to Ni leading to reversible protonation [139] in the presence of a strong acid. Additional [NiFe] complexes [42, 125] and [NiFeSe] complexes [141] have been suggested in recent years. The first fully functional [NiFe] hydrogenase mimic that can perform both H_2 evolution and oxidation under normal conditions was published by Ogo et al. [95]. The structure of this complex is characterized by triethylphosphite ligands attached to iron. Neutron-scattering analysis revealed that in Ogo's complex the hydride binds to the Fe and not to the Ni atom.

Morokuma et al. [47] recently reported a detailed mechanistic study of the electron/hydride transfer of Ogo's [NiFe] mimic. Figure 1 shows the catalytic cycle proposed by Morokuma and co-workers, which starts with the removal of acetonitrile from Fe. The resulting [NiFe] complex can accommodate the binding of H_2 to Fe (complex **A**). Complex **A** undergoes a heterolytic H–H bond cleavage with the help of the Lewis base MeO^-, forming an intermediate hydride complex (complex **B**). The catalytic cycle completes with hydride transfer from complex **B**. However, there are some important open questions with regard to the key factors determining the catalytic efficiency, (1) how strong are the Fe ⋯ H_2 interaction in complex **A** and the Fe ⋯ H^- interaction in **B**; and (2) can the Fe ligands, in particular, the ligand in trans-position to H_2 and H^- influence the strength of these interactions; (3) can these ligands also influence the strength of the H–H bond of H_2 in complex **A**? This information can be used as a valuable basis for the design and fine tuning of future [NiFe] biomimetic catalysts.

To answer these questions, we studied Ogo's [NiFe] mimic, which we simplified by changing the three triethylphosphite ($P(OEt)_3$) groups to phosphine (PH_3) ligands. Fe and its ligands form a quasi-octahedron with the two PH_3 groups in a horizontal plane, one PH_3 group in a trans-position relative to the H_2 ligand in complex **A** and the H^- ligand in complex **B**. As shown in Fig. 2, the PH_3 in trans-position, (complex **A5** and **B5**, respectively) was systematically replaced in our calculations by 16 different ligands, (complexes **A1–A4**, **A6–A17** and complexes **B1–B4**, **B7–B17**, respectively) selected from the spectroscopic series [20, 121] and the trans effect series in transition metal complexes [17, 18, 41, 104] to cover a wide range of ligands with different electronic character. The ligands were ordered according to their influence of the H–H bond strength in complexes **A**, e.g., ligand **L1** leads to complex **A1** with the strongest H–H bond and ligand **L17** to complex **A17** with the weakest H–H bond investigated in this work.

Computational methods frequently determine the strength of a chemical bond via molecular orbital approaches [45, 58, 81], dissociation energies [33, 71, 91], or energy decomposition methods [83, 126]. However, these approaches provide more qualitative rather than quantitative results [25, 145]. Therefore, we used local vibrational force constants based on the local mode analysis of Konkoli and Cremer [66, 144, 145] to quantitatively assess the intrinsic bond strength of the Fe–H and H–H bonds in complexes **A1–A17** and that of the Fe–H bond in complexes **B1–B17**. The local mode analysis has been successfully applied to characterize covalent bonds [54, 74, 76, 78, 114, 120, 144] and weak chemical

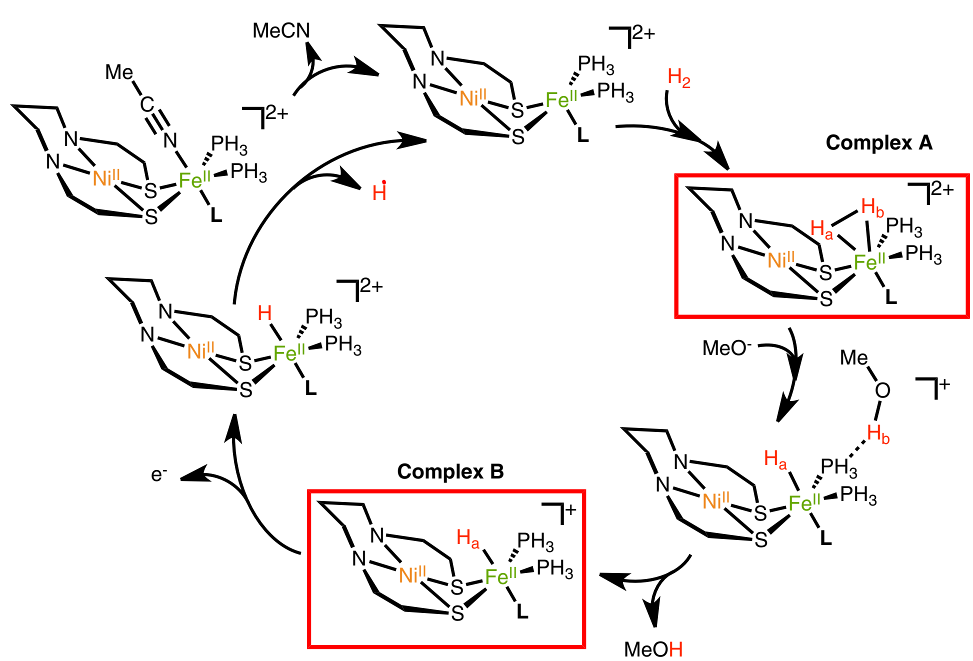

Fig. 1 Catalytic cycle of the [NiFe] hydrogenase mimic used in study. This catalytic cycle is a modified version of the catalytic cycle proposed by Morokuma et al. [47] being based on Ogo's mimic (the three $P(OEt)_3$ groups of Ogo's mimic were replaced with PH_3 ligands). Complex **A** and complex **B**, the focus of this work are shown in the red boxes. H_a is the H atom closer to Ni and forming the hydride bond with Fe in complex **B**. For a definition of ligands **L**, see Fig. 2

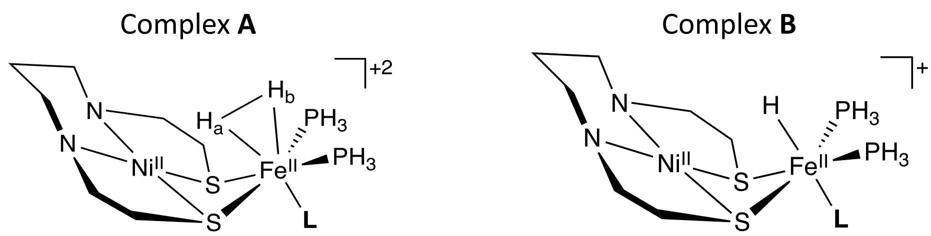

Ligand	SCN^-	CO	NO_2^-	CN^-	PH_3	ON	CH_3^-	$C_6H_5^-$	$C_2H_5^-$	C_2H_4	NH_3	H_2S	NCS^-	F^-	Cl^-	OH^-	H_2O
Complex **A**	**A1**	**A2**	**A3**	**A4**	**A5**	**A6**	**A7**	**A8**	**A9**	**A10**	**A11**	**A12**	**A13**	**A14**	**A15**	**A16**	**A17**
Complex **B**	**B1**	**B2**	**B3**	**B4**	**B5**	**B6**	**B7**	**B8**	**B9**	**B10**	**B11**	**B12**	**B13**	**B14**	**B15**	**B16**	**B17**

Fig. 2 Definition of ligands **L** used in this work for complexes **A1**–**A17** and **B1**–**B17**. The ligands are numbered according to decreasing H–H bond strength in complexes **A1**–**A17**, e.g., **L1** corresponds to the complex with the strongest and **L17** to the complex with the weakest H–H bond

interactions such as halogen [96, 98, 99], chalcogen [97, 100, 118], pnicogen [115–117], and tetrel interactions [113] as well as H bonding [35, 53, 55, 129]. Local vibrational force constants could also clearly illustrate that a shorter bond is not always a stronger bond [27, 67, 68, 74]. In this study, we used the local mode analysis to target the following tasks:

1. Utilizing the local mode force constant k^a values of the Fe–H and H–H bonds to derive a bond strength order (BSO n) for all Fe–H and H–H bonds in complexes **A1**–**A17** and all Fe–H bonds in complexes **B1**–**B17**;
2. To determine the covalent character of the Fe–H and H–H bonds using the Cremer–Kraka criterion [21, 24, 73];
3. To explore which ligand **L** leads to the weakest/strongest H–H bonds and Fe–H bonds in complexes **A1**–**A17** and how the Fe–H and H–H bond strengths are related;
4. To introduce a new metal–ligand electronic parameter (MLEP) [26, 56, 119] for the general evaluation of the Fe–H bond strength in iron complexes and iron hydrides.

The results of this work are presented in the following order: Sect. 2 describes the quantum chemical methods and computational tools employed in this work. Results and their discussion are presented in Sect. 3. The last section highlights the major outcome of our study, draws conclusions and gives a future perspective.

2 Computational methods

Density functional theory (DFT) [62, 64, 65, 87] was utilized for all geometry optimizations and frequency calculations performed in this study. All calculations were carried out with the BP86 functional [9, 102] and Dunning's cc-pVTZ basis set [142] using an ultrafine integral grid [40]. The effective performance of the BP86 functional for transition metal complexes was discussed in a recent study of Bühl and Kabrede [13] who showed that BP86 provides the best geometries for transition metal complexes compared with other DFT functionals. In addition, BP86 provides vibrational frequencies in good agreement with experiment [3, 39, 124]. This functional has also been used in recent studies of [NiFe] complexes [47, 101].

All complexes **A1**–**A17** and **B1**–**B17** were studied with C_s symmetry and confirmed via frequency calculations as local minima. Complex **B5** the simplification of Ogo's originally synthetic compound [95] was calculated as a cation, and **A5** as a double cation. The charges of the other complexes in the **A** and **B** series were determined according to the charge of ligand **L**. The elucidation of the covalent character of the Fe–H_a, Fe–H_b, and H–H bonds in complexes **A**, and that of the Fe–H bond in complexes **B** was performed via the Cremer–Kraka criterion [23, 24, 73]. Additionally, the topological analysis of the Laplacian of the electron density, $\nabla^2\rho(\mathbf{r})$, and the gradient vector field $\Delta\rho(\mathbf{r})$ [4, 5, 73] were used to clarify how the H_2 unit is attached to iron. Natural bond orbital (NBO) charges and orbital occupancy [110] were evaluated for further characterization. This material is contained in the supplementary material, Tables S1 and S2.

To ensure that a single-reference description is valid for complexes **A** and **B**, we applied the T1 diagnostic [50] for DLPNO–CCSD(T)/aug-cc-pVTZ [6] test calculation-based DFT geometries. Additionally, for complex **B5**, CASPT2 calculations [1, 34, 105] with a 10 electron-10 orbital space confirmed that a single-reference description is valid. For the complex **B** series, we determined singlet-triplet splittings. The results of our calculations revealed that all complexes **B** have a singlet ground state, in agreement with the results of Morokuma et al. [47], Delcey et al. [28] and Jayapal et al. [48]. Singlet-triplet splittings and the local mode force constants for the triplet states are collected in the supplementary material, Tables S5–S7.

To derive a quantitative measure for Fe–H and H–H bonding, we drew upon vibrational spectroscopy. The normal vibrational motions of a molecule in its equilibrium provide a wealth of information about its structure, stability, and the strength of its bonds. However, normal vibrational modes in a molecule are always coupled, therefore they cannot be used as a direct measure of bond strength. There are two coupling mechanisms between the vibrational modes, *electronic coupling* associated with the potential energy content of a vibrational mode and *mass coupling* associated with the kinetic energy content [25, 145]. The electronic coupling between the normal vibrational modes is caused by the off-diagonal elements of the force constant matrix **F** and can be eliminated by diagonalizing **F**, i.e., solving the fundamental equation of vibrational spectroscopy [140],

$$\mathbf{F^q}\,\mathbf{D} = \mathbf{G}^{-1}\,\mathbf{D}\,\boldsymbol{\Lambda} \tag{1}$$

where $\mathbf{F^q}$ is the force constant matrix in internal coordinates **q** and **G** is the Wilson mass-matrix. Matrix **D** collects the normal mode eigenvectors $\mathbf{d}_\mu$ and the diagonal matrix $\boldsymbol{\Lambda}$ collects the vibrational eigenvalues $\lambda_\mu = 4\pi^2c^2\omega_\mu$, where ω_μ represents the harmonic vibrational frequency of mode $\mathbf{d}_\mu$ given in reciprocal cm, c is the speed of light, and $\mu = (1\ldots N-L$; N: number of atoms in the molecule, $L=5$ for linear and 6 for nonlinear molecules).

Solution of Eq. 1 leads to the diagonal force constant matrix **K** given in normal coordinates **Q** which is free of electronic coupling:

$$\mathbf{K^Q} = \mathbf{D}^{\dagger}\mathbf{F^q}\mathbf{D} \tag{2}$$

However, mass coupling is still present when the electronic coupling is eliminated by solving the Wilson equation, a fact which has frequently been overlooked. In 1998, Konkoli and Cremer [66] determined for the first time local, mass-decoupled vibrational modes $\mathbf{a}_i$ directly from normal vibrational modes $\mathbf{d}_\mu$ by solving the mass-decoupled Euler–Lagrange equations. The subscript i specifies an internal coordinate q_i and the local mode is expressed in terms of normal coordinates **Q** associated with force constant matrix $\mathbf{K^Q}$ of Eq. 2. The local vibrational modes are unique [145] and they can be based on either calculated or experimentally determined vibrational frequencies via [22, 27, 66–69]

$$\mathbf{a}_i = \frac{\mathbf{K}^{-1}\mathbf{d}_i^{\dagger}}{\mathbf{d}_i\,\mathbf{K}^{-1}\,\mathbf{d}_i^{\dagger}} \tag{3}$$

To each local mode $\mathbf{a}_i$, a corresponding local mode frequency ω_i^a, local mode mass $G_{i,i}^a$, and a local force constant k_i^a can be defined [66]. The local mode frequencies can be uniquely connected to the normal mode frequencies via an adiabatic connection scheme [145]. The local mode frequency ω_i^a is defined by:

$$(\omega_i^a)^2 = \frac{G_{i,i}^a\,k_i^a}{4\pi^2c^2} \tag{4}$$

and the force constant k_i^a by:

$$k_i^a = \mathbf{a}_i^{\dagger}\,\mathbf{K}\,\mathbf{a}_i \tag{5}$$

Local mode force constants, contrary to normal mode force constants, have the advantage of being independent of the choice of the coordinates used to describe the molecule in question and in contrast to local vibrational frequencies they are independent of the atomic masses. They are extremely sensitive to differences in the electronic structure (e.g., caused by changing a substituent) and they capture only electronic effects. Local mode force constants k^a which are related to bond lengths, can be used as quantitative measure of the intrinsic bond strength recently shown by Zou and Cremer [144]. Therefore, the local vibrational force constants provide a unique tool for assessing the strength of a chemical bond via vibrational spectroscopy.

It is convenient to base the comparison of the bond strength of a series of molecules on bond strength order (BSO) n rather than on a direct comparison for local force constant values. Both are connected via a power relationship according to the generalized Badger rule derived by Cremer et al. [76]

$$\mathrm{BSO}\;n = a\,(k^a)^{\,b} \tag{6}$$

The constants a and b in Eq. 6 can be determined via two reference compounds with known k^a values and the requirement that for a zero force constant the BSO n is zero. The same level of theory has to be applied for all compounds of the series to be discussed, in this work BP86/cc-pVTZ.

For the H–H power relationship we used as reference molecules H_2 with k^a 5.532 [mDyn/Å] and BSO n 1.0 and H_2^+ with k^a 1.086 [mDyn/Å] and BSO n 0.5 leading to constants a and b of 0.48274 and 0.42575, respectively.

$$\mathrm{BSO}\;n(\text{H-H}) = 0.48274\,(k^a)^{\,0.42575} \tag{7}$$

For the Fe–H power relationship, we used as references the low-spin complex $[Fe(CO)_5]$ in which one axial CO ligand was replaced by H^- and H_2, respectively. The C_{3v} symmetric $[Fe(CO)_4H]$ complex led to a k^a (F–H) value of 1.954 mDyn/Å and the C_s symmetric $[Fe(CO)_4H_2]$ complex led to a k^a (F–H) value of 1.024 mDyn/Å. As BSO n values for these two references, the corresponding Mayer bond orders [88–90] n(Mayer) 0.6454 and n(Mayer) 0.4775 were used, respectively. This led to the constants $a = 0.47225$ and $b = 0.46630$.

$$\mathrm{BSO}\;n(\text{Fe-H}) = 0.47225\,(k^a)^{\,0.46630} \tag{8}$$

Table 1 Bond distances, local modes, electron and energy density at the bond critical point for the H–H, Fe–H_a, Fe–H_b bonds of Complexes **A1**–**A17**

Complex	Ligand	Character	H–H					Fe–H_a					Fe–H_b				
			R(H–H)	k^a	BSO n	$\rho(\mathbf{r}_b)$	$H(\mathbf{r}_b)$	R(Fe–H_a)	k^a	BSO n	$\rho(\mathbf{r}_b)$	H(r)	R(Fe–H_b)	k^a	BSO n	$\rho(\mathbf{r}_b)$	$H(\mathbf{r}_b)$
A1	SCN^-	π-donor	0.839	2.284	0.686	1.458	− 1.385	1.677	0.819	0.430			1.667	0.849	0.438	0.593	− 0.143
A2	CO	σ-donor, π-acceptor	0.836	2.268	0.684	1.465	− 1.398	1.701	0.818	0.430			1.677	0.851	0.438	0.562	− 0.121
A3	NO_2^-	σ-donor, π-acceptor	0.849	2.023	0.652	1.424	− 1.328	1.654	0.693	0.398	0.602	− 0.159	1.654	0.693	0.398	0.602	− 0.159
A4	CN^-	σ-donor, π-acceptor	0.863	1.748	0.612	1.380	− 1.265	1.669	0.943	0.460			1.633	1.021	0.477	0.624	− 0.202
A5	PH_3	σ-donor	0.864	1.649	0.597	1.380	− 1.269	1.650	0.974	0.466			1.626	1.043	0.482	0.638	− 0.186
A6	ON	σ-donor, π-acceptor	0.865	1.637	0.595	1.381	− 1.269	1.632	0.908	0.451			1.625	1.020	0.477	0.657	− 0.232
A7	CH_3^-	σ-donor	0.874	1.564	0.584	1.339	− 1.206	1.667	0.924	0.455			1.624	1.039	0.481	0.644	− 0.231
A8	$C_6H_5^-$	σ-donor	0.870	1.552	0.582	1.349	− 1.222	1.685	0.785	0.422			1.636	0.933	0.457	0.625	− 0.218
A9	$C_2H_5^-$	σ-donor	0.875	1.517	0.576	1.337	− 1.201	1.658	0.884	0.446			1.624	0.999	0.472	0.648	− 0.230
A10	C_2H_4	π-donor	0.883	1.464	0.568	1.335	− 1.201	1.606	1.107	0.495	0.702	− 0.248	1.594	1.203	0.515	0.706	− 0.231
A11	NH_3	σ-donor	0.885	1.409	0.559	1.325	− 1.186	1.606	1.187	0.512	0.690	− 0.230	1.593	1.275	0.529	0.686	− 0.226
A12	H_2S	σ-donor	0.881	1.401	0.557	1.332	− 1.198	1.616	1.119	0.498	0.677	− 0.200	1.598	1.182	0.511	0.683	− 0.224
A13	NCS^-	σ-donor	0.892	1.292	0.538	1.303	− 1.153	1.621	1.156	0.505			1.586	1.268	0.528	0.701	− 0.275
A14	F^-	π-donor	0.904	1.179	0.518	1.272	− 1.106	1.605	1.250	0.524	0.677	− 0.211	1.577	1.331	0.540	0.717	− 0.291
A15	Cl^-	π-donor	0.903	1.157	0.514	1.271	− 1.107	1.608	1.210	0.516			1.576	1.306	0.535	0.722	− 0.294
A16	OH^-	π-donor	0.909	1.086	0.500	1.258	− 1.084	1.602	1.201	0.514	0.683	− 0.215	1.576	1.273	0.529	0.727	− 0.306
A17	H_2O	σ-donor	0.906	1.081	0.499	1.271	− 1.108	1.582	1.326	0.539	0.736	− 0.274	1.569	1.376	0.548	0.732	− 0.281
References																	
$\mathbf{H_2}$	H–H		0.751	5.532	1.000	1.772	− 1.921										
$\mathbf{H_2^+}$	H–H^+		1.134	1.086	0.500	0.554	− 0.432										
$\mathbf{Fe(CO)_4H}$	Fe–H							1.543	1.954	0.645	0.793	− 0.447					
$\mathbf{Fe(CO)_4H_2}$	Fe–H							1.609	1.024	0.478	0.765	− 0.240	1.609	1.024	0.478	0.765	− 0.240

Computed at BP86/cc-pVTZ. Bond distances R in [Å], local mode force constants k^a in [mDyn/Å], bond strength order (BSO n), electron density $\rho(\mathbf{r}_b)$ at the bond critical point $\mathbf{r}_b$ in [e/Å^3] and energy density $H(\mathbf{r}_b)$ at the bond critical point $\mathbf{r}_b$ in [Hartree/Å^3]

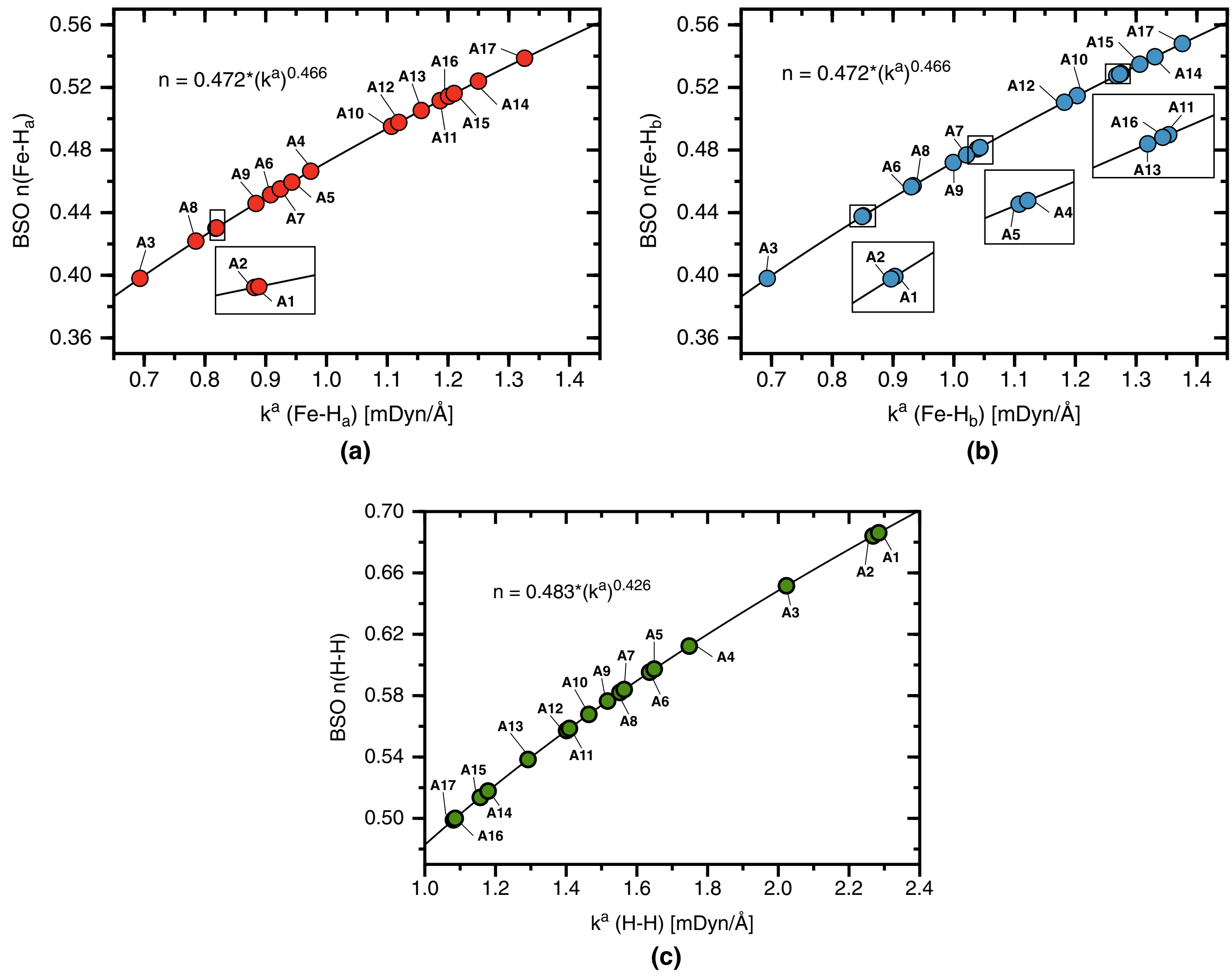

Fig. 3 Power relationship between the relative bond strength order BSO n and the local stretching force constants k^a of the Fe–H_a bonds (**a**), the Fe–H_b bonds (**b**), and the H–H bonds (**c**), in complexes **A1**–**A17**. For a numbering of complexes, see Fig. 2. Calculated at the BP86/cc-pVTZ level of theory

All DFT and CASPT2 calculations were carried out with Gaussian16 [38]. The local mode force constants, k^a were calculated with COLOGNE2018 [79]. The topological analysis of the electronic density was performed with AIMAll (Ver. 17.11.14) [60], DLPNO–CCSD(T) calculations as well as the calculation of the Mayer bond orders were performed with the ORCA 4.0.1 program package [93].

3 Results and discussion

Section 3.1 is dedicated to complexes **A1**–**A17** and Sect. 3.2 to complexes **B1**–**B17**. In Sect. 3.3 the Fe–H metal ligand electronic parameter MLEP is introduced.

3.1 Complexes A1–A17

As shown in Fig. 1, the first key step of the catalytic cycle is H_2 coordination to the [NiFe] hydrogenase mimic. Geometry optimizations revealed that the H_2 molecule only coordinates to the Fe and not the Ni atom, primarily because there is no vacant orbital in the axial direction on the Ni site. This is in agreement with the study of Morokuma et al. [47]. There are two possible binding modes to iron, H_2 can coordinate to Fe side-on, e.g., via one H atom or as η^2-dihydrogen, in which both H atoms are at a comparable distance from the Fe atom. We identified for all complexes **A1**–**A17**, η^2-dihydrogen coordination as the most stable complex form with the Fe–H_b distance being equal or slightly shorter than the Fe–H_a distance. This seems to contradict the fact that the Fe–H_b is the bond to be broken. However, it is line with

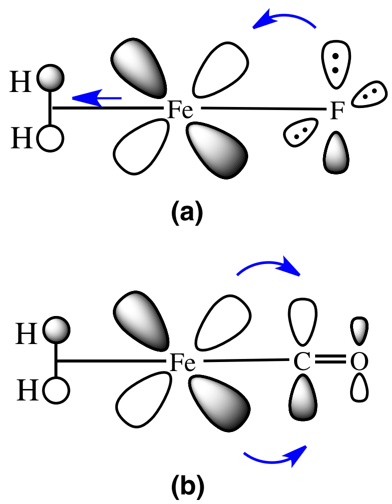

Fig. 4 **a** π-donation from F^{-} to the Fe center in complex **A14**, **b** π-back-donation from the Fe d_{xz} orbital to the π^* orbital of CO in complex **A2**

our observation, that bond breaking often starts with charge polarization so that the bond being attacked becomes first stronger and even shorter before it is broken [77]. Fe–H_b bond lengths range from 1.677 Å in **A2** to 1.569 Å, in **A17**. It is noteworthy that the Fe–H_b distance in **A17** is considerably shorter than that in the reference compound $[Fe(CO)_4H_2]$ (1.609 Å) and closer to hydride reference compound $[Fe(CO)_4H]$ (1.543 Å), see Table 1. As revealed by the electron density and energy density data in Table 1, all Fe–H_a and Fe–H_b bonds in complexes **A1**–**A17** are of covalent nature according to the Cremer–Kraka criterion [23, 24, 73]. For some complexes a Fe–H_a bond path was not found, which will be discussed in more detail below.

The H–H bond lengths in complexes **A1**–**A17** increase from 0.839 Å in complex **A1** to 0.909 Å in complex **A16**. Compared to the H–H bond length of 0.751 Å in H_2, this is a considerable increase. However, all complexes **A** can still be classified as a *Kubas type* (normal H_2) complexes [49, 80] in which the interaction between two hydrogen atoms is still intact, i.e., the H–H bond distance is less than 1.5 Å [46]. In addition, according to the Cremer–Kraka criterion [23, 24, 73] all H–H bonds are of covalent nature.

The BSO n values of the Fe–H_a and Fe–H_b bonds in complexes **A1**–**A17** are compared in Fig. 3a, b. They cover a range of 0.430 to 0.539 for the Fe–H_a bonds and 0.438 to 0.548 for the Fe–H_b bonds, respectively. The BSO n values of reference ligand PH_3 (**A5**) are with 0.466 and 0.482 in the middle range showing that our set of ligands represents both weakening and strengthening of the Fe–H bonds. It is noteworthy that our simplified mimic does not suffer from substantial steric effects as revealed by the corresponding local force constants (k^a of Fe–H_a and Fe–H_b for **A5** are 0.974 and 1.043 mDyn/Å, respectively, compared to 0.898 and 0.964 mDyn/Å for Ogo's original complex, justifying the use of **A5** in this work). σ- or π-donor ligands such as H_2O or F^{-} lead to a strengthening of the Fe–H_a and Fe–H_b bonds whereas ligands with σ donor/π acceptor character such as CO or CN^{-} weaken the Fe–H_a and Fe–H_b bonds. The opposite is found for the H–H bonds as reflected by the BSO n values shown in Fig. 3c.

As illustrated in Fig. 4a for complex **A14**, π donation from F^{-} to Fe leads to a transfer of charge from the Fe d_{xz} orbital to the σ^* orbital of the H_2 unit; thus, weakening the H–H bond, e.g., leading to an increase in the H_2 bond length and a decrease in the bond strength as also reflected by the data in Table 1. For ligands with π-back donation such as CO (complex **A2**) shown in Fig. 4b, charge can be transferred back from the Fe d_{xz} orbital into the π^* ligand orbital. In this way, the electron density of Fe is polarized in a direction of the ligand away from the σ^* orbital of the H_2 unit leading to a stronger H–H bond. There is one notable exception, ligand SCN^{-}. Known as π-donor [12, 111, 133], this ligand should lead to a weakening of the H–H bond. However, complex **A1** has the strongest H–H bond of all complexes **A** investigated in this work. The NBO analysis revealed that most of electron density transfer from the Fe center in complex **A1** occurs to the S atoms of cysteine thiolate subunit with almost no electron density transfer from the Fe center to the σ^* of H–H bond, resulting in weak Fe–H_a and Fe–H_b, and a strong H–H bonds. This unusual electron transfer is reflected by the Fe–S thioloate bond lengths which are shorter than in the case of complex **A13** with a NCS^{-} ligand, see supplementary material Fig. S1.

According to the Cremer–Kraka criterion, the covalent character of a chemical bond is reflected by a negative value of the energy density $H(\mathbf{r}_b)$ at the bond critical point $\mathbf{r}_b$ [23, 24, 73]. For the H–H bonds in complexes **A1**–**A17**, we find a linear correlation between the local stretching force constant k^a and the electron density $\rho(\mathbf{r}_b)$, see Fig. 5a as well as between the local stretching force constant k^a and the energy density $H(\mathbf{r}_b)$ see Fig. 5b, in this way unifying both, the description of bonding via the local force constant, a potential energy related property and electron density related properties. Largest $\rho(\mathbf{r}_b)$ values corresponding to smallest $H(\mathbf{r}_b)$ values are observed for complexes with the π-back donating ligands such as **A2** and **A3**, and for **A1** in which π-donation occurs predominantly into the bridging sulfur atoms. Complexes with σ- or π-donating ligands weakening the H–H bond via the population of the σ^* orbital of the H_2 unit such as **A16** or **A17** have the smallest $\rho(\mathbf{r}_b)$ and largest $H(\mathbf{r}_b)$ values. The relationship between the local stretching force constant k^a and $\rho(\mathbf{r}_b)$, Fig. 5c and that between k^a

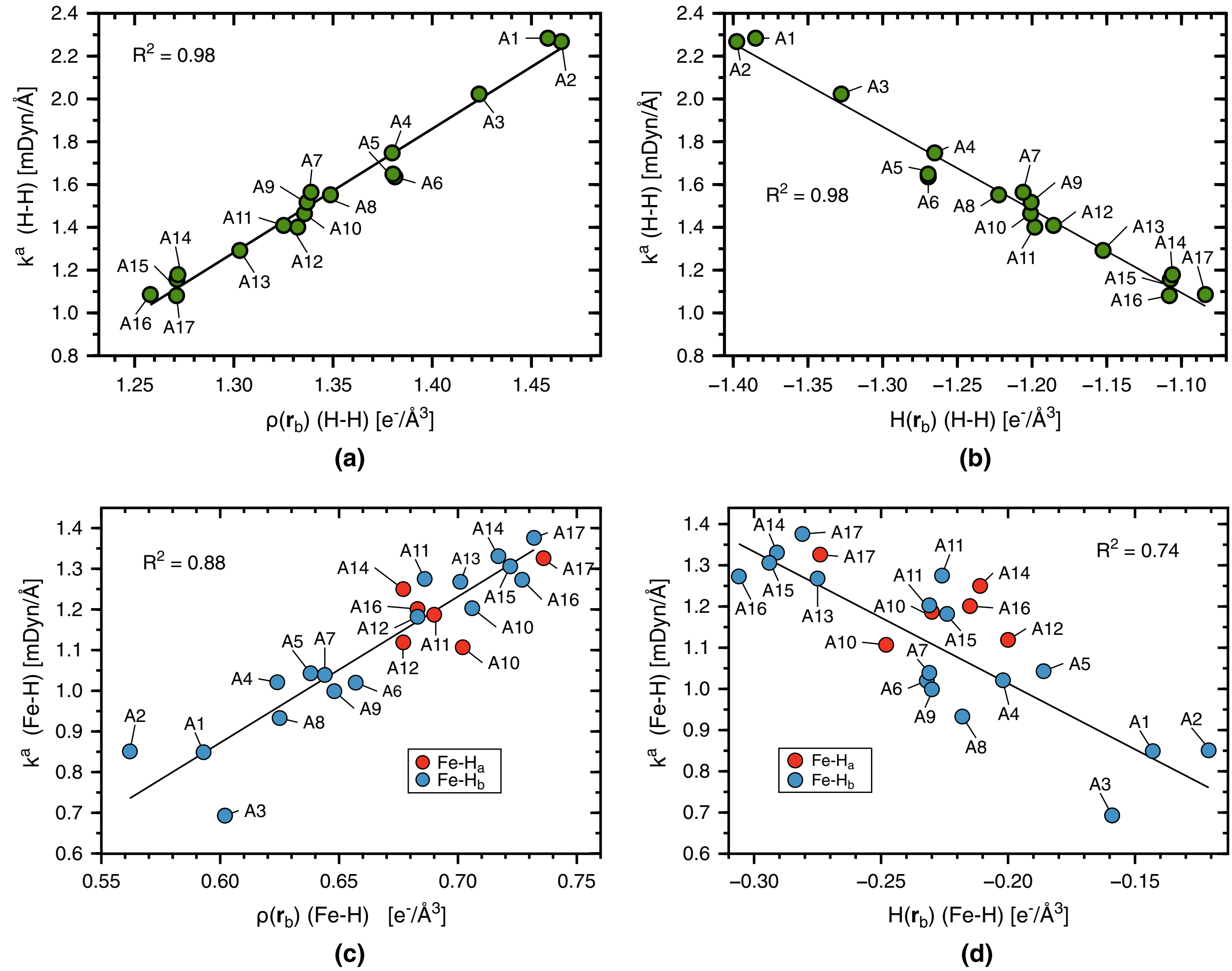

Fig. 5 **a** Relationship between the electron density $\rho(\mathbf{r}_b)$ and the local stretching force constant k^a for the H–H bonds, **b** relationship between with energy density $\mathrm{H}(\mathbf{r}_b)$ and the local stretching force constants k^a for the H–H bonds for the H–H bonds, **c** relationship between the electron density $\rho(\mathbf{r}_b)$ and the local stretching force constants k^a for the Fe–H bonds, and **d** relationship between with energy density $\mathrm{H}(\mathbf{r}_b)$ and the local stretching force constants k^a for the Fe–H bonds for complexes **A1**–**A17**. Calculated at the BP86/cc-pVTZ level of theory. For numbering of the complexes, see Fig. 2

and $\mathrm{H}(\mathbf{r}_b)$, Fig. 5d for the Fe–H bonds is less pronounced. However, it is obvious that the electron density in the Fe–H bonds increases in the complexes **A14**–**A17** and decreases in **A1**–**A3**, which is opposite to what we find for the H–H bonds.

In the following the relationship between changes in H–H and Fe–H bonding caused by the different ligands **L** will be further elucidated. Figure 6a illustrates the inverse relationship between the H–H and Fe–H bond distances, which also holds for the local stretching force constants k^a (H–H) and k^a(Fe–H) as shown in Fig. 6b. k^a values of the Fe–H_a and Fe–H_b bonds increase as the strength of H–H bonds decreases, e.g., weakening of the H–H bond results in an increased interaction of the individual H atoms with the iron center. σ- or π-donation from the ligand to the Fe center strengthens the Fe–H_a and Fe–H_b bonds and facilitates donation from the Fe center via the d_{xz} orbital to the σ^* of the H_2 unit; thus, weakening the H–H bond and preparing the complex for H–H cleavage. In this connection, the question arises how the different ligands influence the energetics of the H_2 binding to the [NiFe] hydrogenase mimic. Activation enthalpies, summarized in Table 2, range from 1.92 kcal/mol for complex **A9** to 4.59 kcal/mol for complex **A8** indicating that there is no direct relationship between the Fe–H bond strengthening/H–H weakening of a ligand and its influence on the barrier of the H_2 binding reaction. However, this is different with regard to the reaction enthalpies for the formation of complex **A**. While the activation enthalpies vary within a small range of 2.67 kcal/mol, the reaction enthalpies

Table 2 Activation energies $\Delta E^{\#}$, reaction energies ΔE_R, activation enthalpies $\Delta H^{\#}$ and reaction enthalpies ΔE_R in (kcal/mol) for H_2 binding to the [NiFe] hydrogenase mimic leading to complex **A**

Complex	Ligand	$\Delta E^{\#}$	ΔE_R	$\Delta H^{\#}$	ΔH_R
A1	SCN^-	2.93	− 9.03	3.26	− 7.89
A2	CO	2.34	− 6.45	2.8	− 3.82
A3	NO_2^-	2.88	− 4.67	3.32	− 2.16
A4	CN^-	2.37	− 9.63	2.74	− 7.11
A5	PH_3	2.50	− 9.10	3.56	− 5.96
A6	ON	2.45	− 10.00	2.98	− 8.57
A7	CH_3^-	3.78	− 8.76	4.05	− 6.13
A8	$C_6H_5^-$	2.73	− 10.33	4.59	− 2.75
A9	$C_2H_5^-$	2.06	− 12.97	1.92	− 6.23
A10	C_2H_4	1.98	− 10.54	2.05	− 8.71
A11	NH_3	1.41	− 11.98	2.36	− 9.97
A12	H_2S	1.41	− 13.34	2.42	− 10.27
A13	NCS^-	2.26	− 13.98	3.35	− 10.71
A14	F^-	2.99	− 16.35	3.29	− 14.53
A15	Cl^-	3.23	− 14.21	3.53	− 11.82
A16	OH^-	2.85	− 12.34	3.19	− 9.80
A17	H_2O	1.61	− 19.62	2.04	− 17.19

Calculated at the BP86/cc-pVTZ level of theory

stretch over a large range from − 2.16 kcal/mol for complex **A3** to − 17.19 kcal/mol for complex **A17**. As indicated in Fig. 6c, there is a trend that ligands strengthening the Fe–H bonds and weakening the H–H bonds lead to more stable complexes such as **A17** or **A14**.

As discussed above, we observed η^2-dihydrogen coordination for all complexes **A1**–**A17**, suggesting a three-membered ring topology between the H_2 unit and the iron center with three bond paths between H–H, Fe–H_a and Fe–H_b and a ring critical point, as shown for complex **A17** in Fig. 7a. According to the data in Table 1, this is the case for majority of complexes with σ- or π-donor ligands leading to weak H–H bonds, such as complexes **A10**–**A12**, **A14**, **A16**, and **A17**. These complexes are also the more stable ones according to the reaction enthalpies of Table 2. Complex **A3** falls into this category because of the symmetry leading to two equal Fe–H bonds. For complexes with π-back donation ligands such as **A1**, **A2** and **A4**, we did not find a three-membered ring topology but two bond paths, one between the H–H atoms and one between Fe–H_b as shown for complex **A1** in Fig. 7b, see also Table 1. These complexes are less stable as reflected by the reaction enthalpies of Table 2. We did not encounter any π complex with two bond paths, one between the H atoms and one connecting the mid-point of the H_2 unit with the iron center.

3.2 Complexes B1–B17

In contrast to complexes **A1**–**A17** with H_2 coordination in complexes **B1**–**B17**, there is only one hydrogen atom coordinated to the iron center, e.g., hydride H_a after the heterolytic H–H cleavage by MeO^-, see Fig. 1. Geometry parameters and the Fe–H normal mode frequency for complex **B5** calculated at the BP86/cc-pVTZ level of theory compare well with the experimental values of the original Ogo hydride compound as shown in Table 3. This confirms that our level of theory is sufficient and that our simplified mimic changing the three triethylphosphite ($P(OEt)_3$) groups to phosphine (PH_3) ligands still reproduces the important features of the original complex. The structure of Ogo's hydride complex was determined by the X-ray diffraction, and the frequency of the Fe–H stretching vibration by the infrared spectroscopy [95]. ^{1}H NMR spectroscopy provided evidence for diamagnetism of this molecule, which was also confirmed by Mössbauer spectroscopy and a computational study [47, 63], e.g., confirming a singlet ground state in agreement with our calculated singlet-triplet splittings, see supplementary material Tables S5–S7.

According to the data in Table 4, the Fe–H bond lengths in complexes **B1**–**B17** are in the range of 1.631 Å (complex **B8**) to 1.523 Å (complex **B17**) compared to a value of 1.543 Å in reference compound $Fe(CO)_4H$, and according to the Cremer–Kraka criterion all Fe–H bonds are of covalent nature. The BSO n values of Fe–H bonds in complexes **B1**–**B17** are compared in Fig. 8. They cover the range of 0.506 for complex **B8** to 0.620 for complex **B17** and as such they are on the average stronger than the Fe–H bonds in complexes **A1**–**A17**, as expected.

As for the Fe–H bonds in complexes **A1**–**A17**, we observe that σ- and π-donor ligands strengthen the Fe–H bond. As sketched in Fig. 9a for complex **B17** with the strongest Fe–H bond, the H_2O ligand transfers charge from the oxygen lone pair into the empty Fe d_z^2 orbital which is further transferred into the Fe–H bond strengthening it. On the other hand, ligands with π-back-donation character suppress the polarization of the iron electron density into the direction of the Fe–H bond, leading to weaker Fe–H bonds as shown for the CO ligand of complex **B2** in Fig. 9b. Our findings are in line with other studies [41] explaining the trans effects in transition metals via the electron density donation from ligands to the metal, which are in a trans-position.

Compared with Fe–H bonds in complexes **A1**–**A17**, the correlation between the local stretching force constant k^a and the electron density $\rho(\mathbf{r}_b)$, see Fig. 10a as well as between the local stretching force constant k^a and the energy density $H(\mathbf{r}_b)$, see Fig. 10b is less pronounced. The largest $\rho(\mathbf{r}_b)$ value and smallest $H(\mathbf{r}_b)$ value corresponding

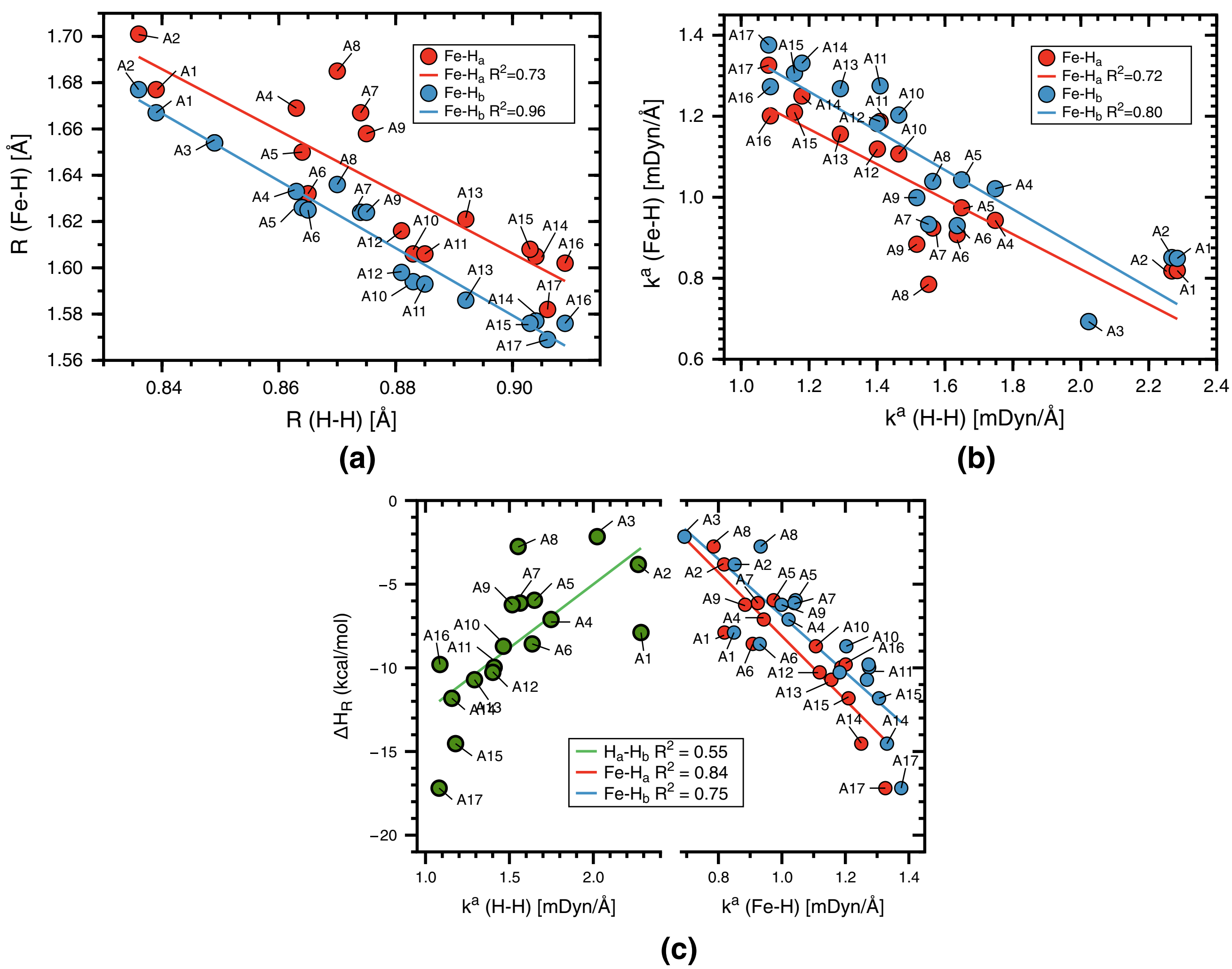

Fig. 6 **a** Relationship between H–H and Fe–H bond distances in the complexes **A1**–**A17**, **b** relationship between the local stretching force constants k^a of the H–H bonds and the Fe–H bonds, **c** relationship between the local stretching force constants k^a of the H–H bonds (left part) and the Fe–H bonds (right part) and the reaction enthalpies for H_2 binding to the [NiFe] hydrogenase mimic, see also Table 2. Calculated at the BP86/cc-pVTZ level of theory. For numbering of the complexes, see Fig. 2

to the strongest Fe–H bond is found for complex **B17** whereas the weakest Fe–H bond with the smallest $\rho(\mathbf{r}_b)$ and largest $H(\mathbf{r}_b)$ value is that of complex **B7** with the CH_3^- ligand in contrast to complexes **A** with the weakest Fe–H bonds for the SCN^- ligand, complex **A1**. The NBO analysis of **B1** (SCN^-) revealed that in contrast to complex **A1** there is no charge transfer from the iron center to the cysteine thiolate subunit, but some back transfer of electron density from the Fe center to the S π^* orbital of thiocyanate group, resulting in a medium strong Fe–H bond. This is in agreement with previous studies suggesting that the SCN^- ligand coordinates to a transition metal predominantly through σ- or π-bonding [111, 133] with a possible of π^*-back donation from the transition metal center to the thiocyanate group [12].

3.3 The Fe–H metal ligand electronic parameter

Experimentalists have used since decades the Tolman electronic parameter (TEP) to describe the strength of metal–ligand (M–L) bonding [130–132]. The TEP is an indirect bond strength measure being defined as the A_1-symmetrical CO stretching frequency of nickel tricarbonyl phosphine complexes of the type L–Ni$(CO)_3$ with L = R_3P. This frequency can be easily identified in the infrared spectrum. Tolman's underlying assumption is that the carbonyl ligand is sensitive to any electronic structure change at the metal atom. Any ligand that increases the electron density at the metal atom converts the latter to a potential nucleophile that shifts negative charge into in the low-lying π^* (CO) orbital. Accordingly, the CO bond is weakened, and the value of

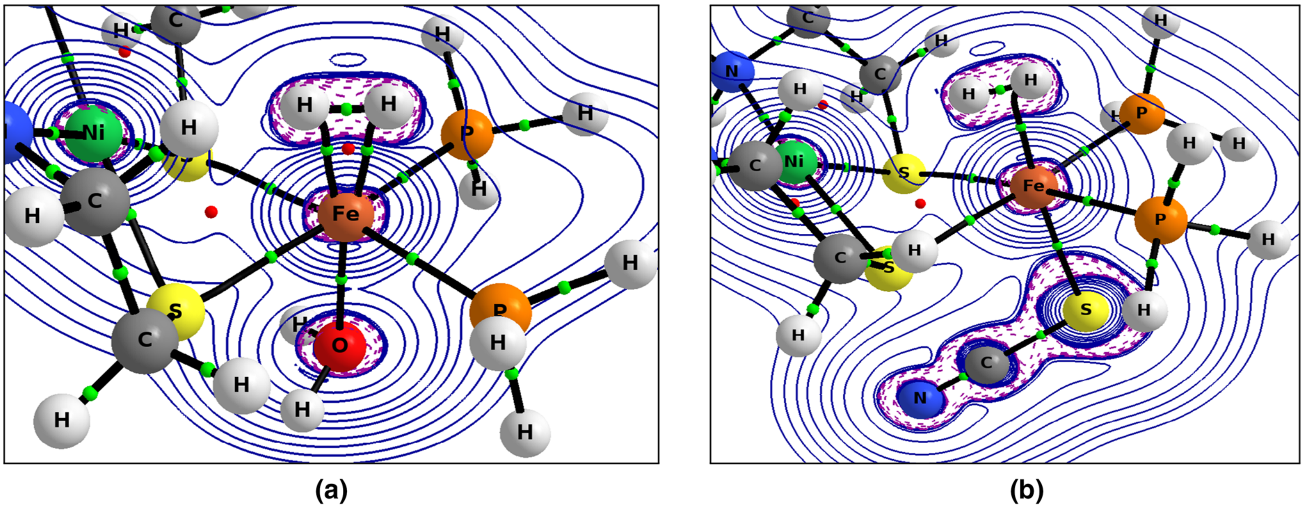

Fig. 7 Laplacian $\nabla^2\rho(\mathbf{r}_b)$ of the electron density distribution $\rho(\mathbf{r}_b)$ of complex **A17** (**a**) and complex **A1** (**b**) in the Cs symmetry plane containing Fe and H_2 unit. Solid black lines indicate bond paths, green dots bond critical points $\mathbf{r}_b$ and red dots ring critical point. Dashed purple lines corresponds to a concentration of charge with $\nabla^2\rho < 0$, and solid blue lines to a depletion of charge with $\nabla^2\rho > 0$

Table 3 Comparison of experimental geometry parameters and normal vibrational frequencies of Ogo's mimic [95] with the calculated values for **B5** complex

	Experiment	BP86/cc-pVTZ
Fe–H distance	1.57 (5) Å	1.566 Å
Ni–H distance	2.16 (4) Å	2.094 Å
Ni–Fe distance	2.7930 (6) Å	2.731 Å
Ni–S_1–Fe angle	75.82 (3)°	73.857°
Ni–S_2–Fe angle	75.76 (3)°	73.857°
Fe–H frequency	1687 cm^{-1}	1670 cm^{-1}

Calculated at BP86/cc-pVTZ

the A_1-symmetrical CO stretching frequency is lowered. This redshift can directly be registered in the infrared spectrum and qualifies the TEP as an indirect descriptor for the metal–ligand bond strength.

Recently, Cremer, Kraka and co-workers showed via an intensive local mode study of a set of 181 nickel-tricarbonyl complexes using both experimental and calculated vibrational frequencies, that the TEP is at best a qualitative parameter that suffers from relatively large mode-mode coupling errors and the basic deficiency that the intrinsic M–L bond strength cannot be quantitatively assessed via the CO stretching frequencies. They suggested to describe the catalytic activity of transition metal complexes $(R)_n$M–L directly utilizing the metal–ligand electronic parameter (MLEP), which they defined as the local stretching force constant of the M–L bond. The MLEP is ideally suited to set up a scale of bond strength orders because it quantitatively assesses both electronic and steric factors. Furthermore, the MLEP can be determined for any metal or transition metal complex, whether it contains CO ligands or not [26, 56, 119]. So far MLEPs were introduced for Pb, Ti, Cr ligand bonds [119], here we introduce the MLEP for Fe–H bonds, represented by the BSO *n*(Fe–H) for easier comparison.

In Fig. 11, the MLEP (values for the 55 Fe–H bonds of complexes **A1**–**A17** and complexes **B1**–**B17** are presented together with the two reference compounds $[Fe(CO)_4H_2]$ and $[Fe(CO)_4H]$. MLEP values stretch over a range of 0.478 to 0.645 showing that Fe–H_a bonds are generally weaker than Fe–H_b bonds in complexes **A1**–**A17** and that the Fe–H hydride bonds in complexes **B1**–**B17** are stronger than their complex **A** counterparts. As a first proof for the general applicability of MLEP(Fe–H), Fig. 11 also includes two iron hydrides, the high spin FeH_2 molecule, the only transition metal dihydride which has been detected so far in the gas phase [70] with Fe–H bonds in the medium strong range, and the diatomic FeH molecule, one of the few molecules found in the sun [16]. FeH has been extensively studied by DeYonker and Allen [29]. Our calculation of the ground state quartet of FeH with a Fe–H distance of 1.530 Å (in good agreement with DeYonker's and Allen's results) identifies the Fe–H bond of this diatomic as the strongest Fe–H bond investigated in this work, with an MLEP value of 0.700. Work is in progress to extend our studies to other Fe–H complexes of interest in catalysis [2, 51, 92] and as functional materials [84].

Table 4 Summary of geometry and vibrational data of the Fe–H bond for Complexes **B1**–**B17**

Complex	Ligand	Character	Fe–H				
			r(Fe–H)	k^a	BSO n	$\rho(\mathbf{r}_b)$	H($\mathbf{r}_b$)
B1	SCN^-	π-donor	1.581	1.416	0.555	0.756	− 0.394
B2	CO	σ-donor, π-acceptor	1.589	1.334	0.540	0.734	− 0.362
B3	NO_2^-	σ-donor, π-acceptor	1.606	1.288	0.531	0.768	− 0.406
B4	CN^-	σ-donor, π-acceptor	1.612	1.292	0.532	0.667	− 0.297
B5	PH_3	σ-donor	1.566	1.495	0.570	0.762	− 0.391
B6	ON	σ-donor, π-acceptor	1.544	1.511	0.572	0.805	− 0.324
B7	CH_3^-	σ-donor	1.628	1.190	0.512	0.642	− 0.279
B8	$C_6H_5^-$	σ-donor	1.631	1.160	0.506	0.680	− 0.322
B9	$C_2H_5^-$	σ-donor	1.578	1.452	0.562	0.763	− 0.404
B10	C_2H_4	π-donor	1.557	1.497	0.570	0.788	− 0.420
B11	NH_3	σ-donor	1.545	1.654	0.597	0.796	− 0.424
B12	H_2S	σ-donor	1.545	1.608	0.589	0.800	− 0.430
B13	NCS^-	σ-donor	1.576	1.463	0.564	0.796	− 0.429
B14	F^-	π-donor	1.573	1.477	0.566	0.726	− 0.352
B15	Cl^-	π-donor	1.557	1.488	0.568	0.751	− 0.378
B16	OH^-	π-donor	1.596	1.472	0.566	0.696	− 0.325
B17	H_2O	σ-donor	1.523	1.792	0.620	0.844	− 0.474
Reference							
Fe(CO)$_4$H	Fe–H		1.543	1.954	0.645	0.793	− 0.447

Computed at BP86/cc-pVTZ. Bond distances R [Å], local mode force constant, k^a [mDyn/Å], bond strength order, BSO n, electron density distribution, $\rho(\mathbf{r}_b)$ [e/Å^3] and energy density, H($\mathbf{r}_b$) [Hartree/Å^3]

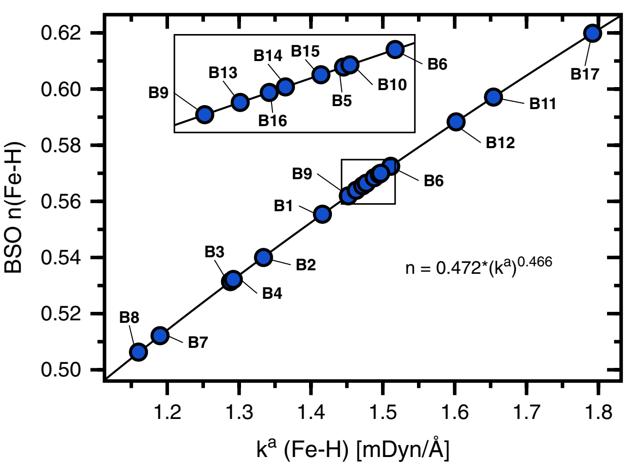

Fig. 8 Power relationship between the relative bond strength order BSO n and the local stretching force constant k^a of the Fe–H bonds in complexes **B1**–**B17**. For a numbering of complexes, see Fig. 2. Calculated at the BP86/cc-pVTZ level of theory

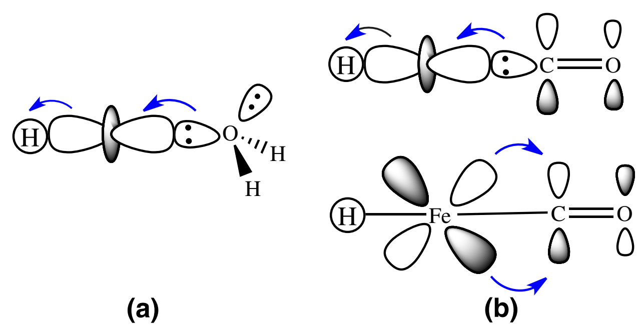

Fig. 9 **a** σ-donation of the H_2O lone pair into the Fe d_z^2 orbital for complex **B17**, **b** σ-donation and π-back-donation from the Fe d_{xz} orbital to the π^* orbital of CO in complex **B2**

4 Conclusions

In this work, we investigated the strength of the H^- and H_2 interaction with the Fe atom of a [NiFe] hydrogenase mimic, and how this interaction can be modulated by changing the Fe ligand **L** in trans-position relative to H^- and H_2. We used as a quantitative measure of bond strength local vibrational force constants and related bond strength orders BSO n derived from the Konkoli–Cremer local modes, complemented by the topological analysis of the electronic density and the Natural Bond Orbital analysis. 17 different ligands were investigated utilizing density functional theory calculations, including σ-donor ligands such as CH_3^-, $C_2H_5^-$, NH_3, and H_2O, π-donor ligands such as Cl^-, F^-, and OH^-, and σ-donor/π-acceptor ligands such as CN^-, and CO. Our study led to the following conclusions:

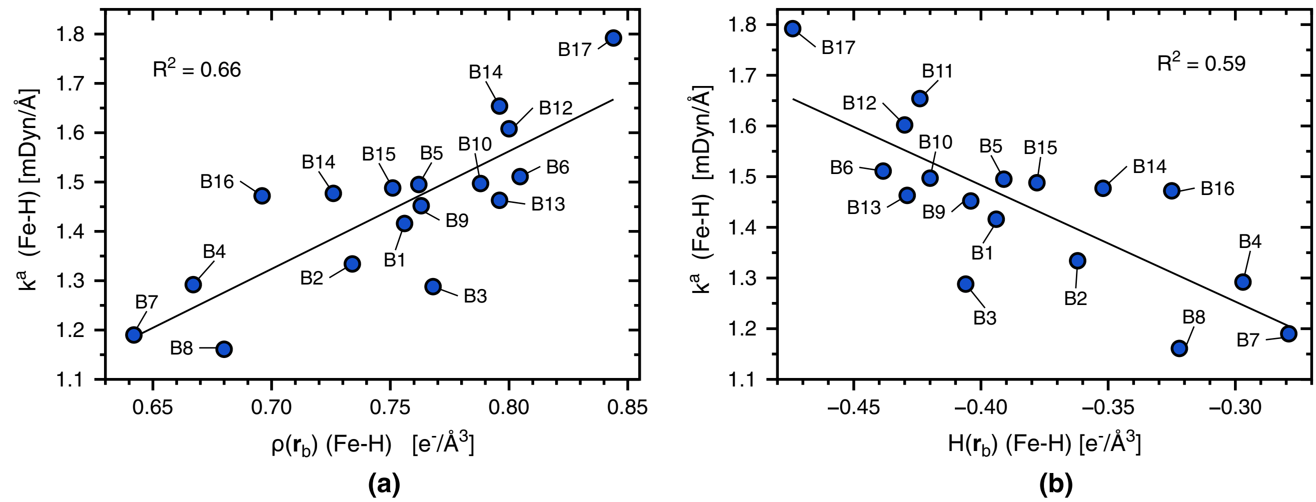

Fig. 10 **a** Relationship between the electron density $\rho(\mathbf{r}_b)$ and the local stretching force constant k^a for the Fe–H bonds, **b** relationship between with energy density $H(\mathbf{r}_b)$ and the local stretching force constants k^a for the Fe–H bonds in the complexes **B1**–**B17**. Calculated at the BP86/cc-pVTZ level of theory. For numbering of the complexes, see Fig. 2

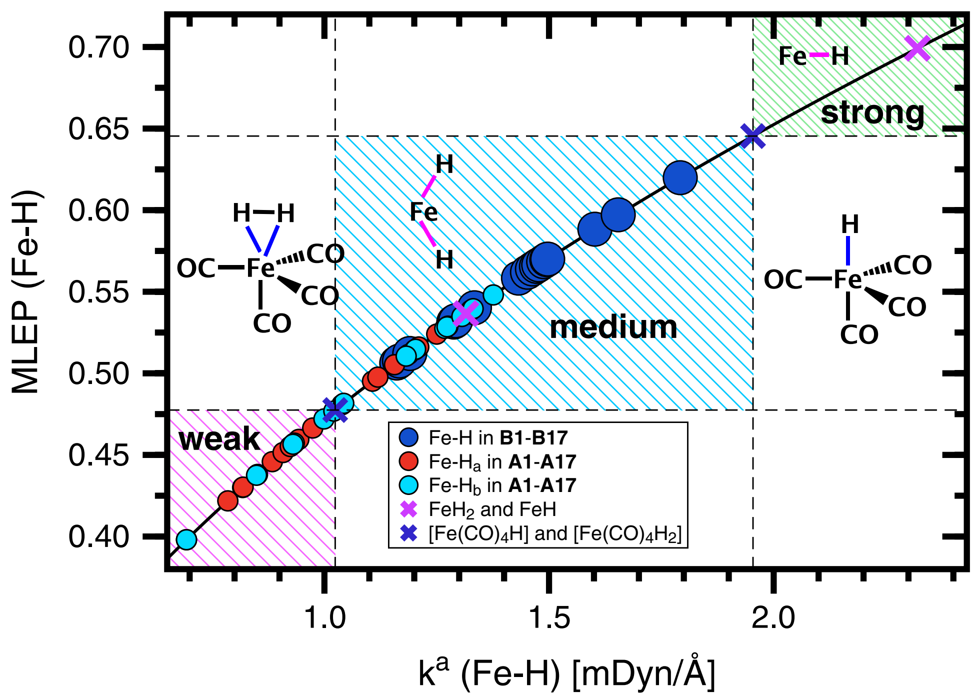

Fig. 11 The Fe–H metal electronic parameter MLEP(Fe–H) corresponding to BSO n(Fe–H) derived from the local Fe–H stretching force constants k^a via Eq. 8. Regions of weak, medium and strong Fe–H bonds are indicated by colored shading

1. Calculated BSO n values clearly reveal that the strength of the Fe–H and H–H bonds in [NiFe] complexes can be modulated by trans ligand substitution. σ- or π-donor ligands increase the strength of the Fe–H bonds for both Fe–H_a and Fe–H_b bonds in complexes **A1**–**A17** and Fe–H bonds in complexes **B1**–**B17**, while σ-donor/π-acceptor ligands lead to Fe–H weakening. The H–H bonds in **A1**–**A17** show the opposite behavior, π-acceptor ligands strengthen and σ- or π-donor ligands weaken the H–H bonds, e.g., weakening of the H–H bond results in an increased interaction of the individual H atoms with the iron center. The covalent nature of all Fe–H and H–H bonds was confirmed with the Cremer–Kraka criterion of covalent bonding.
2. The inverse relationship between Fe–H and H–H bond weakening/strengthening in complexes **A** is also reflected in the complex geometries, weaker and longer Fe–H bonds correspond to stronger and shorter H–H

bonds, and vice versa. This is also reflected in the reaction enthalpies of the H_2 binding reaction. Ligands strengthening the Fe–H bonds and weakening the H–H bonds lead to more stable complexes **A** such as **A17** or **A14**.

3. We identified for all complexes **A** η^2-dihydrogen coordination with Fe–H_b distances being equal or slightly shorter than Fe–H_a distances. Although this seems to contradict the fact that the Fe–H_b is the bond to be broken, this is fully in line with our previous observations, that bond breaking often starts with charge polarization so that the bond being attacked becomes first stronger and even shorter before it is broken.
4. Although all geometries of **A1**–**A17**, suggest η^2-dihydrogen coordination with a three-membered ring topology between the H_2 unit and the iron center with three bond paths between H–H, Fe–H_a and Fe–H_b and a ring critical point, this was predominately found for complexes with σ- or π-donor ligands leading to weak H–H bonds, such as complexes **A10**–**A12**, **A14**, **A16**, and **A17**, in line with their greater stability. For complexes with π-back donation ligands such as **A1**, **A2** and **A4**, we did not find a three-membered ring topology but two bond paths, one between the H–H atoms and one between Fe–H_b.
5. We derived a metal ligand electronic parameter MELP(Fe–H) classifying the 55 Fe–H bonds of complexes **A** and **B** and showed its first application to iron hydrides.

In summary, our study provides new valuable guidelines how to modulate the strength of the H^- and H_2 interactions with the Fe atom in [NiFe] hydrogenase mimics, influencing the complex stability and the catalytic efficiency. Currently, we are exploring the detailed mechanism of H_2 binding and heterolytic cleavage under the influence of different ligands **L** utilizing the Unified Reaction Valley Approach (URVA) developed in our group [25, 36, 72, 75, 146].

Acknowledgements This work was finally supported by the National Science Foundation, Grant CHE 1464906. We thank SMU for providing excellent computational resources.

References

1. Andersson K, Malmqvist PÅ, Roos BO, Sadlej AJ, Wolinski K (1990) Second-order perturbation theory with a CASSCF reference function. J Phys Chem 94(14):5483–5488
2. Aoto YA, de Lima Batista AP, Köhn A, de Oliveira-Filho AGS (2017) How to arrive at accurate benchmark values for transition metal compounds: computation or experiment? J Chem Theory Comput 13(11):5291–5316
3. Assefa MK, Devera JL, Brathwaite AD, Mosley JD, Duncan MA (2015) Vibrational scaling factors for transition metal carbonyls. Chem Phys Lett 640:175–179
4. Bader RFW (1990) Atoms in molecules—a quantum theory. Oxford University Press, Oxford
5. Bader RFW, Carroll MT, Cheeseman JR, Chang C (1987) Properties of atoms in molecules: atomic volumes. J Am Chem Soc 109(26):7968–7979
6. Bartlett RJ, Musiał M (2007) Coupled-cluster theory in quantum chemistry. Rev Mod Phys 79(1):291–352
7. Barton BE, Rauchfuss TB (2010) Hydride-containing models for the active site of the nickel–iron hydrogenases. J Am Chem Soc 132(42):14,877–14,885
8. Barton BE, Whaley CM, Rauchfuss TB, Gray DL (2009) Nickel–iron dithiolato hydrides relevant to the [NiFe]-hydrogenase active site. J Am Chem Soc 131(20):6942–6943
9. Becke AD (1988) Density-functional exchange-energy approximation with correct asymptotic behavior. Phys Rev A 38:3098–3100
10. Breglia R, Greco C, Fantucci P, De Gioia L, Bruschi M (2018) Theoretical investigation of aerobic and anaerobic oxidative inactivation of the [NiFe]-hydrogenase active site. Phys Chem Chem Phys 20:1693–1706
11. Breglia R, Greco C, Fantucci P, De Gioia L, Bruschi M (2019) Reactivation of the ready and unready oxidized states of [NiFe]-hydrogenases: mechanistic insights from DFT calculations. Inorg Chem 58:279–293
12. Buda C, Kazi AB, Dinescu A, Cundari TR (2005) Stability studies of transition–metal linkage isomers using quantum mechanical methods. Groups 11 and 12 transition metals. J Chem Inf Model 45:965–970
13. Bühl M, Kabrede H (2006) Geometries of transition–metal complexes from density-functional theory. J Chem Theory Comput 2(5):1282–1290
14. Burgdorf T, Lenz O, Buhrke T, van der Linden E, Jones AK, Albracht SPJ, Friedrich B (2005) [NiFe]-hydrogenases of Ralstonia eutropha H16: modular enzymes for oxygen-tolerant biological hydrogen oxidation. J Mol Microbiol Biotechnol 10(2–4):181–196
15. Canaguier S, Field M, Oudart Y, Pécaut J, Fontecave M, Artero V (2010) A structural and functional mimic of the active site of NiFe hydrogenases. ChemCommun 46(32):5876–5878
16. Carroll PK, McCormack P (1972) The spectrum of FeH: laboratory and solar identification. Astrophys J 177:L33
17. Chval Z, Sip M, Burda JV (2008) The trans effect in square-planar platinum(II) complexes—a density functional study. J Comput Chem 29(14):2370–2381
18. Coe BJ, Glenwright SJ (2000) Trans-effects in octahedral transition metal complexes. Coord Chem Rev 203:5
19. Crabtree GW, Dresselhaus MS (2008) The hydrogen fuel alternative. MRS Bull 33(4):514–516
20. Crabtree RH (2005) The organometallic chemistry of the transition metals, vol 18. Wiley-Interscience, New York
21. Cremer D (1987) New ways of analyzing chemical bonding. In: Maksic ZB (ed) Modelling of structure and properties of molecules. Ellis Horwood, Chichester, p 125
22. Cremer D (1998) Møller–Plesset perturbation theory. In: Schleyer P, Allinger N, Clark T, Gasteiger J, Kollman P, Schaefer H III, Schreiner P (eds) Encyclopedia of computational chemistry. Wiley, New York, pp 1706–1735
23. Cremer D, Kraka E (1984) Chemical bonds without bonding electron density? Does the difference electron-density analysis suffice for a description of the chemical bond? Angew Chem Int Ed 23(8):627–628

24. Cremer D, Kraka E (1984) A description of the chemical bond in terms of local properties of electron density and energy. Croat Chem Acta 57:1259–1281
25. Cremer D, Kraka E (2010) From molecular vibrations to bonding, chemical reactions, and reaction mechanism. Curr Org Chem 14:1524–1560
26. Cremer D, Kraka E (2017) Generalization of the tolman electronic parameter: the metal–ligand electronic parameter and the intrinsic strength of the metal–ligand bond. Dalton Trans 46(26):8323–8338
27. Cremer D, Larsson JA, Kraka E (1998) New developments in the analysis of vibrational spectra on the use of adiabatic internal vibrational modes. In: Parkanyi C (ed) Theoretical and computational chemistry. Elsevier, Amsterdam, pp 259–327
28. Delcey MG, Pierloot K, Phung QM, Vancoillie S, Lindh R, Ryde U (2014) Accurate calculations of geometries and singlet-triplet energy differences for active-site models of [NiFe] hydrogenase. Phys Chem Chem Phys 16(17):7929–7938
29. DeYonker NJ, Allen WD (2012) Taming the low-lying electronic states of FeH. J Chem Phys 137(23):234,303
30. Dole F, Fournel A, Magro V, Hatchikian EC, Bertrand P, Guigliarelli B (1997) Nature and electronic structure of the Ni-X dinuclear center of Desulfovibrio gigas hydrogenase. Implications for the enzymatic mechanism. Biochem 36(25):7847–7854
31. Dong G, Phung QM, Pierloot K, Ryde U (2018) Reaction mechanism of [NiFe] hydrogenase studied by computational methods. Inorg Chem 57(24):15,289–15,298
32. Esmieu C, Raleiras P, Berggren G (2018) From protein engineering to artificial enzymes biological and biomimetic approaches towards sustainable hydrogen production. Sustain Energy Fuels 2:724–750
33. Fang Z, Vasiliu M, Peterson KA, Dixon DA (2017) Prediction of bond dissociation energies/heats of formation for diatomic transition metal compounds: CCSD(T) works. J Chem Theory Comput 13(3):1057–1066
34. Finley J, Malmqvist PÅ, Roos BO, Serrano-Andrés L (1998) The multi-state CASPT2 method. Chem Phys Lett 288(2–4):299–306
35. Freindorf M, Kraka E, Cremer D (2012) A comprehensive analysis of hydrogen bond interactions based on local vibrational modes. Int J Quantum Chem 112(19):3174–3187
36. Freindorf M, Tao Y, Sethio D, Cremer D, Kraka E (2018) New mechanistic insights into the Claisen rearrangement of chorismate—a Unified Reaction Valley Approach study. Mol Phys 117(9–12):1172–1192 https://doi.org/10.1080/00268976.2018.1530464
37. Frey M, Robson R, Cammack R (2001) Hydrogen as a fuel: learning from nature. Taylor and Francis, London
38. Frisch MJ, Trucks GW, Schlegel HB, Scuseria GE, Robb MA, Cheeseman JR, Scalmani G, Barone V, Petersson GA, Nakatsuji H, Li X, Caricato M, Marenich AV, Bloino J, Janesko BG, Gomperts R, Mennucci B, Hratchian HP, Ortiz JV, Izmaylov AF, Sonnenberg JL, Williams-Young D, Ding F, Lipparini F, Egidi F, Goings J, Peng B, Petrone A, Henderson T, Ranasinghe D, Zakrzewski VG, Gao J, Rega N, Zheng G, Liang W, Hada M, Ehara M, Toyota K, Fukuda R, Hasegawa J, Ishida M, Nakajima T, Honda Y, Kitao O, Nakai H, Vreven T, Throssell K, Montgomery JA Jr, Peralta JE, Ogliaro F, Bearpark MJ, Heyd JJ, Brothers EN, Kudin KN, Staroverov VN, Keith TA, Kobayashi R, Normand J, Raghavachari K, Rendell AP, Burant JC, Iyengar SS, Tomasi J, Cossi M, Millam JM, Klene M, Adamo C, Cammi R, Ochterski JW, Martin RL, Morokuma K, Farkas O, Foresman JB, Fox DJ (2016) Gaussian16 Revision A.03. Gaussian Inc., Wallingford
39. Gao X, Li N, King RB (2018) Heterometallic bonding between a first row transition metal and a third row transition metal: the cyclopentadienyliron rhenium carbonyls $CpFeRe(CO)_n$ (n = 7, 6, 5). Polyhedron 145:231–238
40. Gräfenstein J, Izotov D, Cremer D (2007) Avoiding singularity problems associated with meta-GGA (generalized gradient approximation) exchange and correlation functionals containing the kinetic energy density. J Chem Phys 127(21):214,103
41. Guégan F, Tognetti V, Joubert L, Chermette H, Luneau D, Morell C (2015) Towards the first theoretical scale of the trans effect in octahedral complexes. Phys Chem Chem Phys 18(2):982–990
42. Harrison DJ, Lough AJ, Fekl U (2018) A new structural model for NiFe hydrogenases: an unsaturated analogue of a classic hydrogenase model leads to more enzyme-like Ni–Fe distance and interplanar fold. Acta Crystallogr E 74(9):1222–1226
43. Helm ML, Stewart MP, Bullock RM, DuBois MR, DuBois DL (2011) A synthetic nickel electrocatalyst with a turnover frequency above 100,000 s^{-1} for H_2 production. Science 333(6044):863–866
44. Hexter SV, Grey F, Happe T, Climent V, Armstrong FA (2012) Electrocatalytic mechanism of reversible hydrogen cycling by enzymes and distinctions between the major classes of hydrogenases. Proc Natl Acad Sci 109(29):11,516–11,521
45. Hiberty PC, Danovich D, Shurki A, Shaik S (1995) Why does benzene possess a D_{6h} symmetry? A quasiclassical state approach for probing π-bonding and delocalization energies. J Am Chem Soc 117:7760–7768
46. Hush NS (1997) Relationship between H–D spin–spin coupling and internuclear distance in molecular hydrogen complexes. J Am Chem Soc 119(7):1717–1719
47. Isegawa M, Sharma AK, Ogo S, Morokuma K (2018) Electron and hydride transfer in a redox-active NiFe hydride complex: a DFT study. ACS Catal 8(11):10,419–10,429
48. Jayapal P, Robinson D, Sundararajan M, Hillier IH, McDouall JJW (2008) High level ab initio and DFT calculations of models of the catalytically active Ni–Fe hydrogenases. Phys Chem Chem Phys 10(13):1734–1738
49. Jean Y, Eisenstein O, Volatron F, Maouche B, Sefta F (1986) Interaction between d6 ML_5 metal fragments and hydrogen: η^2-H_2 vs. dihydride structure. J Am Chem Soc 108(21):6587–6592
50. Jiang W, DeYonker NJ, Wilson AK (2012) Multireference character for 3d transition–metal-containing molecules. J Chem Theory Comput 8(2):460–468
51. Jones NO, Beltran MR, Khanna SN, Baruah T, Pederson MR (2004) Hydrogen adsorption and magnetic behavior of Fe_n and Co_n clusters: controlling the magnetic moment and anisotropy one atom at a time. Phys Rev B 70(16):165,406
52. Jugder BE, Welch J, Aguey-Zinsou KF, Marquis CP (2013) Fundamentals and electrochemical applications of [NiFe]-uptake hydrogenases. RSC Advances 3(22):8142
53. Kalescky R, Zou W, Kraka E, Cremer D (2012) Local vibrational modes of the water dimer—comparison of theory and experiment. Chem Phys Lett 554:243–247
54. Kalescky R, Kraka E, Cremer D (2013) Identification of the strongest bonds in chemistry. J Phys Chem A 117(36):8981–8995
55. Kalescky R, Kraka E, Cremer D (2013) Local vibrational modes of the formic acid dimer—the strength of the double hydrogen bond. Mol Phys 111(9–11):1497–1510
56. Kalescky R, Kraka E, Cremer D (2013) New approach to Tolman's electronic parameter based on local vibrational modes. Inorg Chem 53(1):478–495
57. Kampa M, Lubitz W, Van Gastel M, Neese F (2012) Computational study of the electronic structure and magnetic properties of the Ni–C state in [NiFe] hydrogenases including the second coordination sphere. J Biol Inorg Chem 17(8):1269–1281
58. Kaupp M, Danovich D, Shaik S (2017) Chemistry is about energy and its changes: a critique of bond-length/bond-strength correlations. Coord Chem Rev 344:355–362

59. Kaur-Ghumaan S, Stein M (2014) Hydrogenases: how close do structural and functional mimics approach the active site? Dalton Trans 43(25):9392–9405
60. Keith TA (2017) AIMAll Version 17.11.14. K Gristmill Software, Overland Park KS, USA (aim.tkgristmill.com)
61. Kikkawa M, Yatabe T, Matsumoto T, Yoon KS, Suzuki K, Enomoto T, Kaneko K, Ogo S (2017) A fusion of biomimetic fuel and solar cells based on hydrogenase, photosystem II, and cytochrome c oxidase. ChemCatChem 9:4024–4028
62. Koch W, Holthausen MC (2001) A chemist's guide to density functional theory, 2nd edn. Wiley-VCH Verlag GmbH, New York
63. Kochem A, Bill E, Neese F, Van Gastel M (2015) Mössbauer and computational investigation of a functional [NiFe] hydrogenase model complex. Chem Commun 51(11):2099–2102
64. Kohn W, Becke AD, Parr RG (1996) Density functional theory of electronic structure. J Phys Chem 100(31):12,974–12,980
65. Kohn W, Becke AD, Parr RG (2014) Perspective: fifty years of density-functional theory in chemical physics. J Chem Phys 140:18A301-1–18A301-18
66. Konkoli Z, Cremer D (1998) A new way of analyzing vibrational spectra. I. derivation of adiabatic internal modes. Int J Quantum Chem 67(1):1–9
67. Konkoli Z, Cremer D (1998) A new way of analyzing vibrational spectra. III. Characterization of normal vibrational modes in terms of internal vibrational modes. Int J Quantum Chem 67(1):29–40
68. Konkoli Z, Larsson JA, Cremer D (1998) A new way of analyzing vibrational spectra. II. Comparison of internal mode frequencies. Int J Quantum Chem 67(1):11–27
69. Konkoli Z, Larsson JA, Cremer D (1998) A new way of analyzing vibrational spectra. IV. Application and testing of adiabatic modes within the concept of the characterization of normal modes. Int J Quantum Chem 67(1):41–55
70. Körsgen H, Urban W, Brown JM (1999) The infrared spectrum of FeH_2, studied in the gas phase by laser magnetic resonance. J Chem Phys 110(8):3861–3869
71. Kosar N, Ayub K, Gilani MA, Mahmood T (2019) Benchmark DFT studies on C–CN homolytic cleavage and screening the substitution effect on bond dissociation energy. J Mol Model 25(2):47
72. Kraka E (2011) Reaction path Hamiltonian and the unified reaction valley approach. WIREs Comput Mol Sci 1(4):531–556. https://doi.org/10.1002/wcms.65
73. Kraka E, Cremer D (1990) Chemical implication of local features of the electron density distribution. In: Maksic ZB (ed) Theoretical models of chemical bonding. The concept of the chemical bond, vol 2. Springer, Heidelberg, p 453
74. Kraka E, Cremer D (2009) Characterization of CF bonds with multiple-bond character: bond lengths, stretching force constants, and bond dissociation energies. Chem Phys Chem 10(4):686–698
75. Kraka E, Cremer D (2010) Computational analysis of the mechanism of chemical reactions in terms of reaction phases: hidden intermediates and hidden transition states. Acc Chem Res 43(5):591–601. https://doi.org/10.1021/ar900013p
76. Kraka E, Larsson JA, Cremer D (2010) Generalization of the Badger rule based on the use of adiabatic vibrational modes. In: Grunenberg J (ed) Computational spectroscopy. Wiley, New York, pp 105–149
77. Kraka E, Zou W, Freindorf M, Cremer D (2012) Energetics and mechanism of the hydrogenation of XH_n for group IV to group VII elements X. J Chem Theory Comput 8(12):4931–4943. https://doi.org/10.1021/ct300631s
78. Kraka E, Setiawan D, Cremer D (2015) Re-evaluation of the bond length-bond strength rule: the stronger bond is not always the shorter bond. J Comput Chem 37(1):130–142
79. Kraka E, Zou W, Filatov M, Gräfenstein J, Izotov D, Gauss J, He Y, Wu A, Konkoli Z, Polo V, Olsson L, He Z, Cremer D (2018) COLOGNE. See http://www.smu.edu/catco
80. Kubas GJ (2007) Fundamentals of H_2 binding and reactivity on transition metals underlying hydrogenase function and H_2 production and storage. Chem Rev 107(10):4152–4205
81. Lai W, Li C, Chen H, Shaik S (2012) Hydrogen-abstraction reactivity patterns from a to y: the valence bond way. Angew Chem Int Ed 51:5556–5578
82. Lauterbach L, Lenz O (2013) Catalytic production of hydrogen peroxide and water by oxygen-tolerant [NiFe]-hydrogenase during H_2 cycling in the presence of O_2. J Am Chem Soc 135(47):17,897–17,905
83. Levine DS, Head-Gordon M (2017) Energy decomposition analysis of single bonds within Kohn–Sham density functional theory. Proc Natl Acad Sci USA 114(48):12,649–12,656
84. Li HW, Zhu M, Buckley C, Jensen T (2018) Functional materials based on metal hydrides. Inorg 6(3):91
85. Lubitz W, Reijerse E, van Gastel M (2007) [NiFe] and [FeFe] hydrogenases studied by advanced magnetic resonance techniques. Chem Rev 107(10):4331–4365
86. Lubitz W, Ogata H, Ru O, Reijerse E (2014) Hydrogenases. Chem Rev 114:4081–4148
87. Mardirossian N, Head-Gordon M (2017) Thirty years of density functional theory in computational chemistry: an overview and extensive assessment of 200 density functionals. Mol Phys 115(19):2315–2372
88. Mayer I (1983) Charge, bond brder an valence in the ab initio theory. Chem Phys Lett 97:270–274
89. Mayer I (1986) Bond orders and valences from ab initio wave functions. Int J Quantum Chem 29:477–483
90. Mayer I (2007) Bond order and valence indices: a personal account. J Comput Chem 28:204–221
91. Morse MD (2018) Predissociation measurements of bond dissociation energies. Acc Chem Res 52(1):119–126
92. Nakazawa H, Itazaki M (2011) Fe–H complexes in catalysis. In: Plietker B (ed) Iron catalysis: fundamentals and applications. Springer, Berlin, pp 27–81
93. Neese F (2012) The ORCA program system. Wiley Interdiscip Rev Comput Mol Sci 2(1):73–78
94. Ogo S (2009) Electrons from hydrogen. ChemCommun 33(23):3317
95. Ogo S, Ichikawa K, Kishima T, Matsumoto T, Nakai H, Kusaka K, Ohhara T (2013) A functional [NiFe]hydrogenase mimic that catalyzes electron and hydride transfer from H_2. Science 339(6120):682–684
96. Oliveira V, Cremer D (2017) Transition from metal–ligand bonding to halogen bonding involving a metal as halogen acceptor a study of Cu, Ag, Au, Pt, and Hg complexes. Chem Phys Lett 681:56–63
97. Oliveira V, Kraka E (2017) Systematic coupled cluster study of noncovalent interactions involving halogens, chalcogens, and pnicogens. J Phys Chem A 121(49):9544–9556
98. Oliveira V, Kraka E, Cremer D (2016) The intrinsic strength of the halogen bond: electrostatic and covalent contributions described by coupled cluster theory. Phys Chem Chem Phys 18(48):33,031–33,046
99. Oliveira V, Kraka E, Cremer D (2016) Quantitative assessment of halogen bonding utilizing vibrational spectroscopy. Inorg Chem 56(1):488–502
100. Oliveira V, Cremer D, Kraka E (2017) The many facets of chalcogen bonding: described by vibrational spectroscopy. J Phys Chem A 121(36):6845–6862
101. Pan S, Zhao L, Rasika Dias HV, Frenking G (2018) Bonding in binuclear carbonyl complexes $M_2(CO)_9$ (M = Fe, Ru, Os). Inorg Chem 57(13):7780–7791

102. Perdew JP (1986) Density-functional approximation for the correlation energy of the inhomogeneous electron gas. Phys Rev B 33(12):8822–8824
103. Perotto CU, Sodipo CL, Jones GJ, Tidey JP, Blake AJ, Lewis W, Davies ES, McMaster J, Schröder M (2018) Heterobimetallic [NiFe] complexes containing mixed CO/CN-ligands: analogs of the active site of the [NiFe] hydrogenases. Inorg Chem 57(5):2558–2569
104. Pinter B, Van Speybroeck V, Waroquier M, Geerlings P, De Proft F (2013) Trans effect and trans influence: importance of metal mediated ligand–ligand repulsion. Phys Chem Chem Phys 15(40):17,354–17,365
105. Pulay P (2011) A perspective on the CASPT2 method. Int J Quantum Chem 111(13):3273–3279
106. Qiu S, Azofra LM, MacFarlane DR, Sun C (2016) Unraveling the role of ligands in the hydrogen evolution mechanism catalyzed by [NiFe] hydrogenases. ACS Catal 6(8):5541–5548
107. Qiu S, Azofra LM, MacFarlane DR, Sun C (2016) Why is a proton transformed into a hydride by [NiFe] hydrogenases? An intrinsic reactivity analysis based on conceptual DFT. Phys Chem Chem Phys 18(22):15,369–15,374
108. Qiu S, Azofra LM, MacFarlane DR, Sun C (2018) Hydrogen bonding effect between active site and protein environment on catalysis performance in H_2-producing [NiFe] hydrogenases. Phys Chem Chem Phys 20(9):6735–6743
109. Qiu S, Azofra LM, MacFarlane DR, Sun C (2018) Hydrogen bonding effect between active site and protein environment on catalysis performance in H-producing [NiFe] hydrogenases. PhysChemChemPhys 20:6735–6743
110. Reed AE, Curtiss LA, Weinhold F (1988) Intermolecular interactions from a natural bond orbital, donor–acceptor viewpoint. Chem Rev 88(6):899–926
111. Rezaeani F, Ghiasi R, Yousefi M (2018) Theoretical studies of solvent effect on the structure, bonding, and spectroscopic properties (IR, NMR) in the cis-$[Pt(PH_3)_2(NCS)_2]$ and $[Pt(PH_3)_2(SCN)_2]$ linkage isomers. Russ J Phys Chem 92:1748–1756
112. Schilter D, Camara JM, Huynh MT, Hammes-Schiffer S, Rauchfuss TB (2016) Hydrogenase enzymes and their synthetic models: the role of metal hydrides. Chem Rev 116(15):8693–8749
113. Sethio D, Oliveira V, Kraka E (2018) Quantitative assessment of tetrel bonding utilizing vibrational spectroscopy. Molecules 23(11):2763
114. Sethio D, Daku LML, Hagemann H, Kraka E (2019) Quantitative assessment of B–B–B, B–H_b–B, and B–H_t bonds: from BH_3 to $B_{12}H_{12}^{2-}$. ChemPhysChem. https://doi.org/10.1002/cphc.201900364
115. Setiawan D, Cremer D (2016) Super-pnicogen bonding in the radical anion of the fluorophosphine dimer. Chem Phys Lett 662:182–187
116. Setiawan D, Kraka E, Cremer D (2014) Description of pnicogen bonding with the help of vibrational spectroscopy—the missing link between theory and experiment. Chem Phys Lett 614:136–142
117. Setiawan D, Kraka E, Cremer D (2014) Strength of the pnicogen bond in complexes involving group VA Elements N, P, and As. J Phys Chem A 119(9):1642–1656
118. Setiawan D, Kraka E, Cremer D (2015) Hidden bond anomalies: the peculiar case of the fluorinated amine chalcogenides. J Phys Chem A 119(36):9541–9556
119. Setiawan D, Kalescky R, Kraka E, Cremer D (2016) Direct measure of metal–ligand bonding replacing the tolman electronic parameter. Inorg Chem 55(5):2332–2344
120. Setiawan D, Sethio D, Cremer D, Kraka E (2018) From strong to weak NF bonds: on the design of a new class of fluorinating agents. Phys Chem Chem Phys 20(37):23,913–23,927
121. Shriver DF, Atkins PW (2001) Inorganic chemistry, 3rd edn. Oxford University Press, Oxford
122. Siegbahn PEM, Tye JW, Hall MB (2007) Computational studies of [NiFe] and [FeFe] hydrogenases. Chem Rev 107:4414–4435
123. Siegbahn PEM, Tye JW, Hall MB (2007) Computational studies of [NiFe] and [FeFe] hydrogenases. Chem Rev 107(10):4414–4435
124. Silaghi-Dumitrescu I, Bitterwolf TE, King RB (2006) Butterfly diradical intermediates in photochemical reactions of $Fe\ 2(CO)_6(\mu - S_2)$. J Am Chem Soc 128(16):5342–5343
125. Song LC, Yang XY, Cao M, Gao XY, Liu BB, Zhu L, Jiang F (2017) Dithiolato-bridged nickel–iron complexes as models for the active site of [NiFe]-hydrogenases. ChemCommun 53(27):3818–3821
126. Stasyuk OA, Sedlak R, Guerra CF, Hobza P (2018) Comparison of the DFT-SAPT and canonical EDA schemes for the energy decomposition of various types of noncovalent interactions. J Chem Theory Comput 14(7):3440–3450
127. Tai H, Higuchi Y, Hirota S (2018) Comprehensive reaction mechanisms at and nearby the Ni–Fe active sites of [NiFe] hydrogenases. Dalton Trans 47:4408–4423
128. Tang H, Hall MB (2017) Biomimetics of [NiFe]-hydrogenase: nickel- or iron-centered proton reduction catalysis? J Am Chem Soc 139(49):18,065–18,070
129. Tao Y, Zou W, Jia J, Li W, Cremer D (2016) Different ways of hydrogen bonding in water. Why does warm water freeze faster than cold water? J Chem Theory Comput 13(1):55–76
130. Tolman CA (1970) Phosphorus ligand exchange equilibriums on zerovalent nickel. Dominant role for steric effects. J Am Chem Soc 92(10):2953–2956
131. Tolman CA (1972) The 16 and 18 electron rule in organometallic chemistry and homogeneous catalysis. Chem Soc Rev 1(3):337
132. Tolman CA (1977) Steric effects of phosphorus ligands in organometallic chemistry and homogeneous catalysis. Chem Rev 77:313–348
133. Tuan DFT, Reed JW, Hoffmann R (1991) Studies of the linkage and bonding of triatomics in transition metal complexes. J Mol Struct Theochem 232:111–121
134. Ulloa OA, Huynh MT, Richers CP, Bertke JA, Nilges MJ, Hammes-Schiffer S, Rauchfuss TB (2016) Mechanism of H_2 production by models for the [NiFe]-hydrogenases: role of reduced hydrides. J Am Chem Soc 138(29):9234–9245
135. Vidal-Limón AM, Tafoya P, Santini BL, Contreras OE, Aguila SA (2017) Electron transfer pathways analysis of oxygen tolerant [NiFe]-hydrogenases for hydrogen production: a quantum mechanics/molecular mechanics—statistical coupled analysis. Int J Hydrog Energy 42(32):20494–20502
136. Vignais PM, Billoud B (2007) Occurrence, classification, and biological function of hydrogenases: an overview. Chem Rev 107(10):4206–4272
137. Vincent KA, Cracknell JA, Lenz O, Zebger I, Friedrich B, Armstrong FA (2005) Electrocatalytic hydrogen oxidation by an enzyme at high carbon monoxide or oxygen levels. Proc Natl Acad Sci 102:16,951–16,954
138. Vogiatzis KD, Polynski MV, Kirkland JK, Townsend J, Hashemi A, Liu C, Pidko EA (2019) Computational approach to molecular catalysis by 3d transition metals: challenges and opportunities. Chem Rev 119(4):2453–2523
139. Weber K, Krämer T, Shafaat HS, Weyhermüller T, Bill E, Van Gastel M, Neese F, Lubitz W (2012) A functional [NiFe]-hydrogenase model compound that undergoes biologically relevant reversible thiolate protonation. J Am Chem Soc 134(51):20,745–20,755

140. Wilson EB, Decius JC, Cross PCM (1955) Molecular vibrations. The theory of infrared and Raman vibrational spectra. McGraw-Hill, New York
141. Wombwell C, Caputo CA, Reisner E (2015) [NiFeSe]-hydrogenase chemistry. Acc Chem Res 48(11):2858–2865
142. Woon DE, Dunning TH (1995) Gaussian basis sets for use in correlated molecular calculations. V. Core-valence basis sets for boron through neon. J Chem Phys 103(11):4572–4585
143. Zhu W, Marr AC, Wang Q, Neese F, Spencer DJE, Blake AJ, Cooke PA, Wilson C, Schroder M (2005) Modulation of the electronic structure and the Ni–Fe distance in heterobimetallic models for the active site in [NiFe]hydrogenase. Proc Natl Acad Sci 102(51):18280–18285
144. Zou W, Cremer D (2016) C_2 in a box: determining its intrinsic bond strength for the $X^1\Sigma_g^+$ ground state. Chem Eur J 22:4087–4097
145. Zou W, Kalescky R, Kraka E, Cremer D (2012) Relating normal vibrational modes to local vibrational modes with the help of an adiabatic connection scheme. J Chem Phys 137(8):084,114(1–11)
146. Zou W, Sexton T, Kraka E, Freindorf M, Cremer D (2016) A new method for describing the mechanism of a chemical reaction based on the unified reaction valley approach. J Chem Theory Comput 12(2):650–663. https://doi.org/10.1021/acs.jctc.5b01098